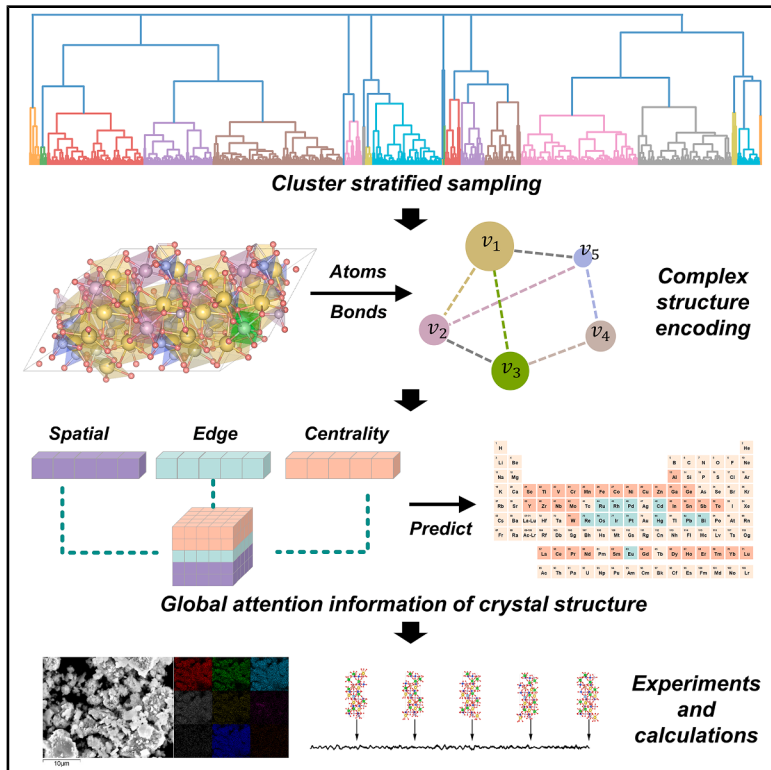


# CGformer: Transformer-enhanced crystal graph network with global attention for material property prediction

## Graphical abstract



## Highlights

- AI model with global attention predicts material properties (CGformer)
- Accelerated discovery of complex crystal structures
- New Na-ion conductors with superior ionic conductivity

## Authors

Kehao Tao, Jiacong Li, Wei He, ..., Feiming Huang, Fuqiang Huang, Jinjin Li

## Correspondence

huangfq@sjtu.edu.cn (F.H.),  
lijinjin@sjtu.edu.cn (J.L.)

## In brief

Designing new materials for better batteries is a major challenge, especially for complex “high-entropy” materials with countless atomic combinations. We developed a novel AI model, CGformer, that looks at the entire crystal structure to accurately predict material properties. By screening nearly 150,000 candidates, our AI identified promising new sodium-ion solid electrolytes. We successfully synthesized these materials, and they showed excellent performance, validating our AI-driven discovery pipeline. This work provides a powerful tool to accelerate the design of next-generation energy materials.



## Improvement

Enhanced performance with innovative design or material control

Tao et al., 2025, Matter 8, 102380  
December 3, 2025 © 2025 Published by Elsevier Inc.

<https://doi.org/10.1016/j.matt.2025.102380>

## Article

# CGformer: Transformer-enhanced crystal graph network with global attention for material property prediction

Kehao Tao,<sup>1,2,3,8</sup> Jiacong Li,<sup>6,7,8</sup> Wei He,<sup>1,2,3</sup> An Chen,<sup>1,2,3</sup> Yanqiang Han,<sup>1,2,3</sup> Feiming Huang,<sup>1,2,3</sup> Fuqiang Huang,<sup>4,5,\*</sup> and Jinjin Li<sup>1,3,9,\*</sup>

<sup>1</sup>National Key Laboratory of Advanced Micro and Nano Manufacture Technology, Shanghai Jiao Tong University, Shanghai 200240, China

<sup>2</sup>Department of Micro/Nano Electronics, School of Electronic Information and Electrical Engineering, Shanghai Jiao Tong University, Shanghai 200240, China

<sup>3</sup>Inner Mongolia Research Institute, Shanghai Jiao Tong University, Hohhot 010010, China

<sup>4</sup>School of Materials Science and Engineering, Shanghai Jiao Tong University, Shanghai 200240, China

<sup>5</sup>Zhangjiang Institute for Advanced Study (ZIAS), Shanghai Jiao Tong University, Shanghai 201210, China

<sup>6</sup>The State Key Laboratory of High Performance Ceramics and Superfine Microstructure, Shanghai Institute of Ceramics, Chinese Academy of Sciences, Shanghai 200050, China

<sup>7</sup>Center of Materials Science and Optoelectronics Engineering, University of Chinese Academy of Sciences, Beijing 100049, China

<sup>8</sup>These authors contributed equally

<sup>9</sup>Lead contact

\*Correspondence: [huangfq@sjtu.edu.cn](mailto:huangfq@sjtu.edu.cn) (F.H.), [lijinjin@sjtu.edu.cn](mailto:lijinjin@sjtu.edu.cn) (J.L.)

<https://doi.org/10.1016/j.matt.2025.102380>

**PROGRESS AND POTENTIAL** Developing next-generation batteries for electric vehicles and grid storage requires new materials that are not only efficient but also safe. Traditional trial-and-error discovery is slow and expensive, especially for complex “high-entropy” materials, which are made by mixing multiple elements and offer vast potential for enhanced performance. The sheer number of possible elemental combinations makes it nearly impossible to test them all in the lab. To solve this, we created an AI model called CGformer. Unlike previous models that only look at immediate neighboring atoms, CGformer uses a “global attention” mechanism to understand how all atoms in a complex crystal interact over long distances. This provides a more complete picture, leading to much more accurate predictions of how well ions, like sodium, can move through the material—a key factor for battery performance.

We used CGformer to rapidly screen nearly 150,000 potential high-entropy materials for sodium-ion batteries, a promising low-cost alternative to lithium-ion. Our AI pinpointed six top candidates, which we then successfully created and tested in the lab. These new materials showed significantly better performance than the original, undoped material, validating our AI-driven approach. The immediate impact is a faster, more intelligent way to design advanced materials. This AI framework is not limited to sodium-ion batteries; it can be adapted to discover other high-performance materials for a wide range of applications, from lithium-ion batteries to thermoelectrics. By accelerating the design cycle, CGformer paves the way for faster breakthroughs in energy storage and other technologies vital for a sustainable future.

## SUMMARY

Crystal graph convolutional neural networks (CGCNNs) pioneered data-efficient property prediction by representing crystals as graphs. However, aggregating messages only between nearest-neighbor atoms makes their receptive field size limited, preventing it from capturing the long-range atomic correlations that govern ion transport in disordered lattices. We introduce CGformer, a transformer-enhanced crystal graph network whose global attention spans all atom-bond interactions, enabling accurate property prediction while excelling in complex lattices. We deployed CGformer on high-entropy Na-ion solid-state electrolytes (HE-NSEs), achieving a 25% reduction in mean absolute error compared to that with CGCNNs. We coupled CGformer with unsupervised clustering to scan 148,995 Na super ionic conductor-type (NASICON-type) dopants and pinpoint 18 compositions. Six top-ranked HE-NSEs were synthesized and verified, revealing room

temperature conductivities up to  $0.256 \text{ mS cm}^{-1}$  and activation energies as low as  $0.235 \text{ eV}$ , surpassing the undoped analog. CGformer provides a transferable framework that can be extended to other advanced materials, including lithium electrode materials, multivalent-ion conductors, and thermoelectric materials.

## INTRODUCTION

Recent advancements in machine learning (ML) have significantly accelerated the discovery and optimization of materials. High-throughput computational approaches combined with ML have facilitated the efficient exploration of material properties, reducing the time and resources required for experimental validation.<sup>1,2</sup> However, the application of artificial intelligence (AI) in complex material structures, such as high-entropy materials, presents unique challenges.<sup>3–5</sup> The inherently complex and multi-dimensional compositional space of high-entropy systems results in sparse and high-dimensional data, which can hinder the training of robust and generalizable ML models. Traditional ML approaches may struggle to capture the intricate interactions between multiple dopants, leading to reduced predictive accuracy. Furthermore, the limited availability of high-quality, labeled data for high-entropy materials exacerbates the difficulty in developing effective models.<sup>6</sup> The dynamic and disordered nature of high-entropy materials also complicates the feature engineering process, as conventional descriptors may not adequately represent the local environments and configurational entropy effects. Consequently, there is a pressing need for the development of advanced AI methodologies, such as transfer learning and active learning,<sup>7–9</sup> tailored specifically to handle the complexity and diversity of high-entropy systems. Moreover, widely utilized material property prediction networks, such as the crystal graph convolutional neural network (CGCNN),<sup>10</sup> atomistic line graph neural network (ALIGNN),<sup>11</sup> and SchNet,<sup>12</sup> have demonstrated exceptional performance and made significant contributions to the field of materials science. These models effectively capture a variety of atomic interactions and chemical environments, enabling accurate predictions of material properties across diverse systems. However, when applied to complex crystal structures and high-entropy material systems, these models exhibit certain limitations. Specifically, they typically account for only a restricted set of atomic interactions and consider limited chemical environments surrounding each atom, thereby failing to fully capture the comprehensive and intricate global information characteristic of high-entropy, complex crystal architectures. To address these challenges, there is an urgent need to develop a computationally efficient neural network architecture that can fully incorporate the interactions between every atom and chemical bond within the crystal structure. Such an advanced model would enable the precise and holistic prediction of material properties in high-entropy environments, addressing the current shortcomings of existing prediction frameworks and facilitating significant advancements in the design and optimization of high-performance materials. Addressing these limitations is essential to fully leverage AI and ML in the design and optimization of high-entropy material systems.

Na-ion solid-state electrolytes (SSEs) represent a pivotal advancement in the development of next-generation energy storage systems, addressing critical challenges associated

with conventional liquid electrolytes.<sup>13–15</sup> Unlike their liquid counterparts, SSEs offer enhanced safety by eliminating flammable and volatile components, thereby significantly reducing the risk of thermal runaway and leakage. This intrinsic safety feature is paramount for large-scale applications, including electric vehicles and grid storage, where reliability and stability are essential.<sup>16–19</sup> Additionally, Na-ion SSEs contribute to increased energy density and longer cycle life, owing to their robust structural integrity and superior ionic conductivity ( $\sigma$ ).<sup>20,21</sup> Among the various SSE candidates, NASICON-type (Na super ionic conductor-type) materials have garnered substantial attention due to their remarkable  $\sigma$  and chemical stability.<sup>22–24</sup> NASICONs, characterized by their versatile crystal structures and ability to accommodate diverse cations, facilitate efficient sodium-ion transport through well-defined pathways, thereby enhancing overall battery performance. Furthermore, the abundance and low cost of sodium compared to lithium make Na-ion batteries (NIBs) an attractive alternative for sustainable energy storage solutions. The integration of SSEs in NIBs not only leverages the economic and environmental benefits of sodium but also paves the way for the commercialization of high-performance, safe, and cost-effective energy storage technologies.<sup>25–28</sup> Consequently, the ongoing research and development of Na-ion SSEs are crucial for overcoming existing limitations and unlocking the full potential of sodium-based energy storage systems, ultimately contributing to the global transition toward sustainable and resilient energy infrastructures.

Building upon the promising potential of Na-ion SSEs, high-entropy Na-ion SSEs (HE-NSEs) present a transformative approach to enhancing  $\sigma$  and structural stability.<sup>6,29</sup> The high-entropy strategy involves doping the NASICON framework with multiple cations, thereby increasing configurational entropy and creating a more disordered yet stable crystal lattice. This multi-elemental doping can facilitate the formation of diverse ion transport pathways, potentially leading to superior  $\sigma$  and enhanced mechanical properties compared to traditional single or dual-doped electrolytes.<sup>30,31</sup> Moreover, the high-entropy concept allows for the fine-tuning of local environments around sodium ions, which can optimize ion migration and reduce activation energy barriers, ultimately improving the overall performance of NIBs.<sup>32,33</sup> However, the design and optimization of HE-NSEs face significant challenges. One of the primary obstacles is the paucity of comprehensive data on the vast compositional space introduced by high-entropy doping. Traditional experimental methods are time consuming and resource intensive, making it difficult to systematically explore and identify optimal compositions.<sup>34,35</sup> Additionally, the complex interactions between multiple dopants can lead to unpredictable phase stability and ionic transport behaviors, complicating the rational design process. Computational modeling and ML techniques hold promise in addressing these challenges by enabling high-throughput screening and predictive analytics.

The objective of this study is to address the challenges posed by data scarcity and structural complexity in high-entropy systems through case-based solutions. We present an AI-driven prediction workflow tailored to these systems that combines unsupervised hierarchical clustering with a transformer-enhanced crystal-property network (CGformer) to accelerate the discovery of HE-NSEs. Whereas conventional convolution-based graph neural networks (GNNs) are confined to local neighborhoods and recurrent models such as long short-term memory networks (LSTMs) struggle with long-range dependencies and parallelization, the transformer architecture with multi-head attention overcomes these limitations. Graphomer extends this global-attention paradigm to graph data, and the CGCNN first demonstrated the efficacy of representing crystals as atom-bond graphs for property prediction. Building on these advances, we fuse Graphomer's attention mechanism with the CGCNN's crystal graph representation, augment it with centrality and spatial encodings, and thereby obtain CGformer, which captures long-range atomic interactions and diffusion pathways with high fidelity even under limited-data conditions. The integration of unsupervised clustering ensures chemically diverse yet information-rich training subsets, while CGformer markedly improves prediction accuracy and generalization for key properties such as diffusion energy barriers in high-entropy materials, laying a robust foundation for large-scale materials screening and high-throughput mechanistic analysis. Furthermore, we establish the largest known dataset of Na-ion diffusion energy barriers ( $E_b$ ) in high-entropy structures based on the crystal structure analysis by Voronoi decomposition (CAVD)<sup>36</sup> and bond valence site energy (BVSE)<sup>37–39</sup> method. By pre-training CGformer on this extensive Na-ion  $E_b$  dataset and subsequently transferring it to the calculated high-entropy dataset, we develop a high-precision prediction network specifically for Na-ion  $E_b$  in high-entropy structures. Ultimately, we predict a highly promising set of structures from a chemical space comprising 148,995 high-entropy NASICONs, which have been effectively validated through climbing image nudged elastic band (CI-NEB) calculations. For the subset of top-ranked candidates, we not only carried out CI-NEB verification but also successfully synthesized these HE-NSEs. The electrochemical testing revealed performance far superior to that of the pristine structures, thereby confirming the robustness and practical utility of our AI-driven workflow. The proposed AI prediction workflow for high-entropy systems successfully identifies the most promising HE-NSEs, significantly reducing the time and experimental costs associated with current research on high-entropy SSEs. Furthermore, this method is not limited to predicting Na-ion  $E_b$  but can be extended to diverse material properties across a broad range of crystal systems. By leveraging CGformer's global-attention architecture, we establish a scalable and transferable framework for accelerating property prediction and materials discovery, with broad applicability to lithium-ion conductors, thermoelectrics, photocatalysts, and other advanced functional materials.

## RESULTS

### Working process

To address the challenges posed by data scarcity and structural complexity in high-entropy systems, an AI-driven prediction

workflow has been designed (Figure 1). In this study,  $\text{Na}_3\text{Zr}_2\text{Si}_2\text{PO}_{12}$  is used as a case to investigate the characteristics of HE-NSEs, where the Zr sites are doped with small amounts of four different elements to form a high-entropy structure. Figure 1A shows the elemental composition of the high-entropy dopants at the Zr sites, with red and blue elements representing potential candidate elements, where red elements denote the final suitable dopants. By doping different elements at the Zr sites, an initial chemical space for HE-NSEs is established. Figure 1B illustrates the primary AI prediction workflow used in this study. First, an unsupervised hierarchical clustering method is applied to cluster HE-NSEs with different compositions. Then, a stratified sampling method is used to extract 30% of the structures from each group to form the HE-NSE dataset for computational analysis. These selected structures undergo structural relaxation and calculations using density functional theory (DFT) and CAVD to generate a low- $E_b$  dataset for HE-NSEs. Moreover, considering the excellent performance of Graphomer in various fields, we integrate it with the CGCNN to develop a new architecture, CGformer. This architecture combines spatial encoding, edge encoding, and centrality encoding and adds a multi-head attention mechanism to enhance the interactions between adjacent atoms, enabling full graph perception. CGformer is pre-trained on the previously calculated Na-ion  $E_b$  dataset, enabling the network to learn relevant knowledge about Na ions. This model is then transferred to the computed HE-NSEs  $E_b$  dataset to create a specialized model capable of accurately predicting Na-ion  $E_b$  in high-entropy NASICON structures for further predictions.

Figure 1C illustrates the primary screening process for HE-NSEs. Initially, there are 45 potential high-entropy dopant elements at the Zr sites in  $\text{Na}_3\text{Zr}_2\text{Si}_2\text{PO}_{12}$  (specific elements listed in Table S1), resulting in a chemical space of 148,995 possible high-entropy structures. Next, some radioactive, highly toxic, and extremely expensive elements, which are difficult to use in large-scale industrial production, are removed, leaving 34 potential dopants (details on the removed elements are provided in Table S2, with further explanation in Note S1). At this point, 40,920 possible structures remain in the HE-NSE chemical space. Additionally, considering that the atomic radius difference between doped elements should not be too large to avoid lattice distortion and internal stress that hinders stable solid solution formation, we set the atomic radius difference between two high-entropy elements to not exceed 50% (Table S3 shows the ionic radii for each high-entropy element in different valence states and the solid solution theory is explained in Note S2) while also considering charge balance for the corresponding valences. This further narrows the chemical space to 826 relatively stable structures. Using the AI workflow depicted in Figure 1B, these structures are hierarchically clustered into 20 groups. From each group, 30% of the structures are selected for optimization and  $E_b$  calculation, forming a dedicated dataset for fine-tuning the CGformer model. Based on the calculated  $E_b$  values, hierarchical clustering identifies the group with the highest proportion of structures with low  $E_b$  values. These structures are considered to have excellent ion diffusion performance, as represented by the 18 candidate structures shown in Figure 1C. The fine-tuned CGformer model is then used to predict the  $E_b$  for this group,

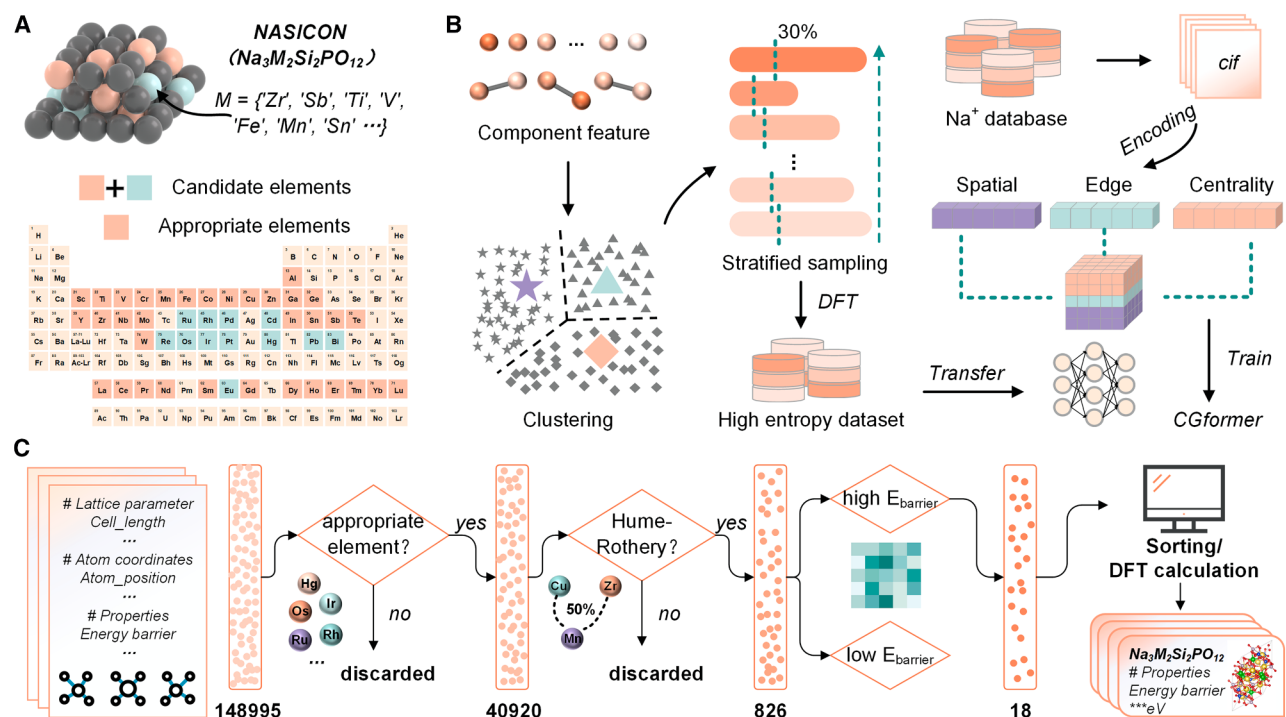


**Figure 1. Workflow diagram**

(A) Schematic illustration of high-entropy element doping at the Zr site in  $\text{Na}_3\text{Zr}_2\text{Si}_2\text{PO}_{12}$ .  
(B) Illustration of the AI prediction process for high-entropy system.  
(C) Schematic of the screening process of HE-NSEs.

and a separate model to assess the thermal stability of Na ions is trained. Using the combination of these two models, six of the most promising structures are selected. These structures have been validated through CI-NEB and *ab initio* molecular dynamics (AIMD) calculations and have also been synthesized experimentally. The results confirm the stability of these new HE-NSEs, which exhibit excellent Na-ion  $\sigma$ . The Na-ion  $\sigma$  of the final batch of HE-NSEs is much greater than that of the undoped control samples, showing excellent superionic  $\sigma$  (a detailed procedural explanation is available in [Figure S1](#) and [Note S3](#)).

In conclusion, this work proposes a novel AI-driven prediction workflow that effectively addresses the challenges of data scarcity and structural complexity in high-entropy systems. By combining advanced neural network architectures with comprehensive datasets, we have successfully accelerated the discovery of HE-NSEs, highlighting the significant potential of AI in advancing high-performance energy storage materials.

### CGformer architecture

Prior to the development of Graphomer, transformer architecture had not achieved significant success within the field of GNNs. However, transformers have demonstrated overwhelming superiority in natural language processing (NLP) and computer vision (CV), sparking interest in leveraging their capabilities within GNNs.<sup>40–42</sup> Based on the standard transformer architecture, Graphomer has achieved state-of-the-art (SOTA) performance across a wide range of graph prediction tasks.<sup>43–45</sup>

Concurrently, Xie et al. developed the CGCNN, which effectively transforms crystal structures into graph representations and accurately predicts various material properties using GNNs.<sup>10</sup> In this study, we integrate both methodologies to introduce the CGformer architecture, which yields highly promising results.

[Figure 2](#) illustrates the primary architecture of CGformer. [Figure 2A](#) depicts the encoding process from crystal structures to crystal graphs. In this process, atoms within the crystal structure are represented as nodes in the graph, and the chemical bonds between atoms are represented as edges. This transformation allows for the extraction of node features and edge features, where node features encompass various elemental properties, such as electric charge and covalent radius, while edge features include interatomic distances, bond types, and crystal symmetry information. By combining these node and edge features, we obtain the input data required for CGformer. [Figure 2B](#) primarily shows the network architecture of CGformer. Initially, the input graph structure undergoes a round of graph convolution to produce a simplified graph structure, thereby reducing the computational load of subsequent network layers and accelerating the training process of CGformer. Building on this, we calculate the centrality encoding and update the node features of the graph structure. The centrality encoding comprises the in-degree and out-degree of each node, which are then integrated into the original node features. Subsequently, each node passes through a multi-head attention module, incorporating edge features and spatial encoding to represent the

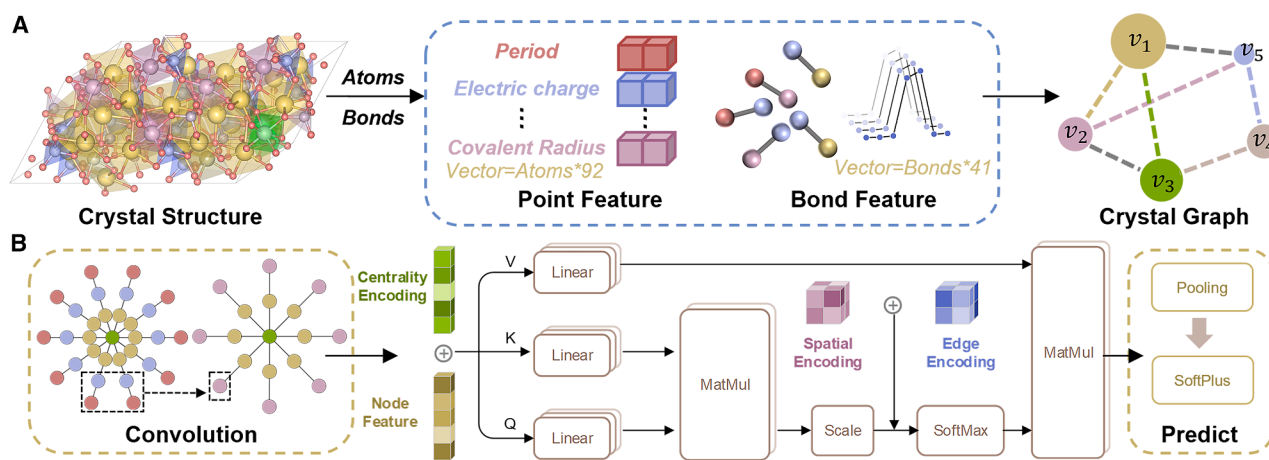


**Figure 2. Architecture diagram of CGformer**

(A) Schematic of the encoding flow from crystal to crystal graph.  
(B) Schematic of the network architecture of CGformer.

positional relationships between nodes. The centrality encoding transforms the average features of neighboring nodes into a summative form, while spatial encoding enables the self-attention mechanism to distinguish between neighboring nodes, facilitating effective message aggregation and enhancing the informational connectivity between different atoms. Finally, the output vectors undergo pooling and activation processes to complete the final property prediction.

The integration of the CGCNN and Graphomer into the CGformer architecture represents a significant advancement in leveraging transformer-based models for material property prediction, demonstrating enhanced accuracy and efficiency in the analysis of HE-NSEs.

### Unsupervised clustering

Currently, both experimental and computational HE-NSEs are extremely scarce. From a computational perspective, a theoretical model of an HE-NSE typically contains nearly 200 atoms, making DFT calculations highly expensive. Therefore, this study employs unsupervised clustering and the CGformer method to ensure the optimal utilization of limited and valuable data while achieving high model accuracy.

Figure 3 illustrates the results of unsupervised hierarchical clustering conducted in this study. Figure 3A displays the dendrogram of the clustering process, where a total of 826 HE-NSEs are clustered into 20 groups, with black dashed lines indicating the partition boundaries. The features used for clustering are based on the 120-dimensional vector designed in a previous work, AlphaMat (detailed descriptions of the features can be found in Note S4). The heatmap of these features is shown in Figure S2, clearly demonstrating that dimensions 104–120 possess distinct discriminative power, effectively distinguishing between different compositions of HE-NSEs. This confirms that the doped high-entropy elements significantly impact the performance of HE-NSEs.

Figure 3B presents the number of structures within each of the 20 groups. The dots in the figure indicate the number of struc-

tures selected for each cluster to be calculated as the HE-NSE dataset (30% of each group). The specific number is given in Table S4. Additionally, the distribution of doped elements in the selected HE-NSE dataset is compared to that of the original dataset, as shown in Figure S3. It is evident that each doped element in the original dataset is represented in the computed dataset, and the quantities and proportions of different elements are largely maintained. This validates the rationality of the stratified sampling method.

After computing the HE-NSE dataset, the distribution of the calculated results within each group is shown in Figure 3C. The median of the computed dataset is used as a threshold, with structures having an  $E_b$  below the threshold considered to possess low  $E_b$ . The top and bottom parts of Figure 3C show the proportion of low- $E_b$  structures within each group and within the computed data of each group. It is observed that in group 13 ( $G_{13}$ ), the proportion of low- $E_b$  structures is the highest, and it is the only group with more than 20%. Almost all the structures in this group are low  $E_b$ . Figure 3D presents a boxplot of the Na-ion  $E_b$  data, where the red box represents the data from  $G_{13}$ , and the brown and orange boxes represent data from outside  $G_{13}$  and all computed  $E_b$  values, respectively. The vertical lines and red boxes within each box represent the median and mean values. The red dashed line shows the average  $E_b$  for  $G_{13}$ . Both the median and average of  $G_{13}$  are significantly lower than those of the other two boxes, indicating that the structures within  $G_{13}$  have excellent superionic  $\sigma$  potential. Therefore, structures within  $G_{13}$  should be the primary focus for further investigation.

The application of unsupervised learning in this study effectively identifies and prioritizes promising HE-NSE structures, thereby enhancing the efficiency and accuracy of discovering high-performance superconductors.

### CGformer prediction

HE-NSEs lack both experimental and computational data, making reliable prediction models crucial for effectively analyzing the

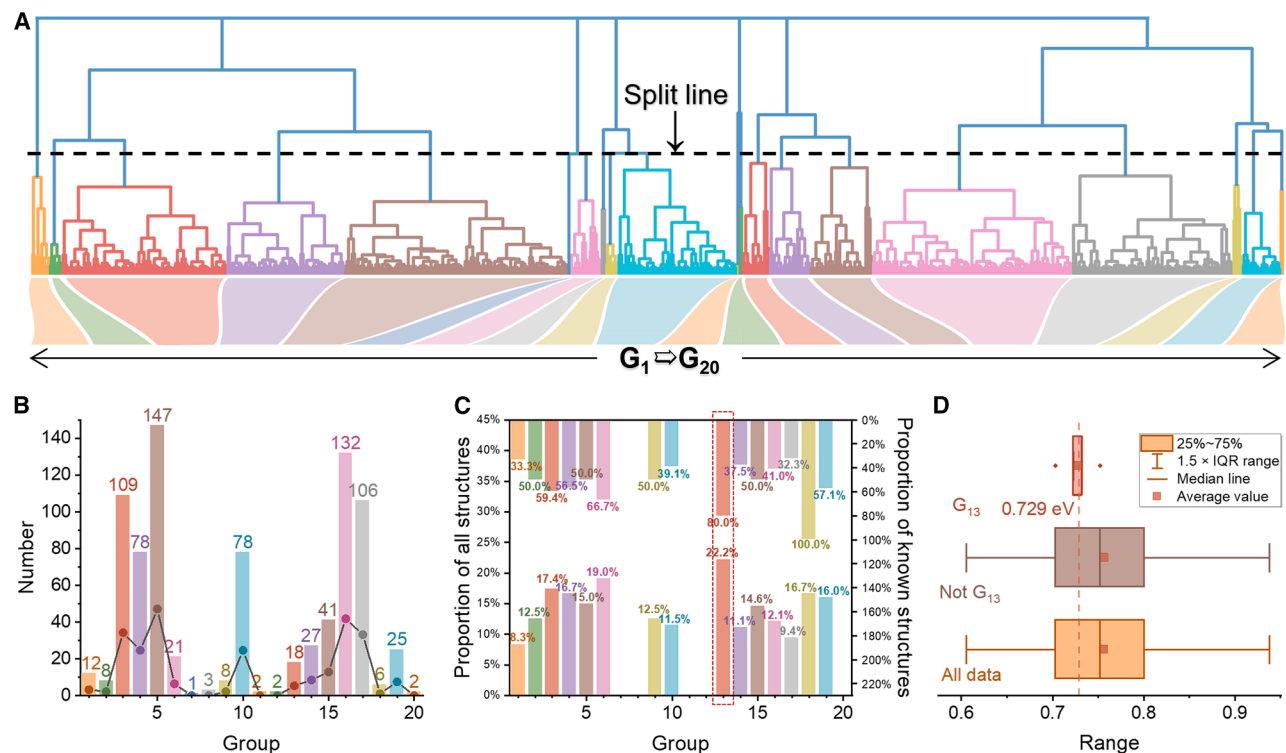


**Figure 3. Diagram of the unsupervised clustering results**

- (A) Schematic diagram of the clustering results, a total of 20 groups are clustered, where the black dotted line represents the splitting line.
- (B) Bar graph of the number of each group, where the dots represent the 30% portion of each group, that is, the number of stratified samples.
- (C) Fraction of structures with low  $E_b$  in each group and the fraction of structures with low  $E_b$  in the known structures of each group.
- (D) Boxplot of the calculated  $E_b$  data for Na-ion diffusion in a high-entropy structure. There are calculated data in  $G_{13}$ , data not in  $G_{13}$ , and all calculated data, respectively.

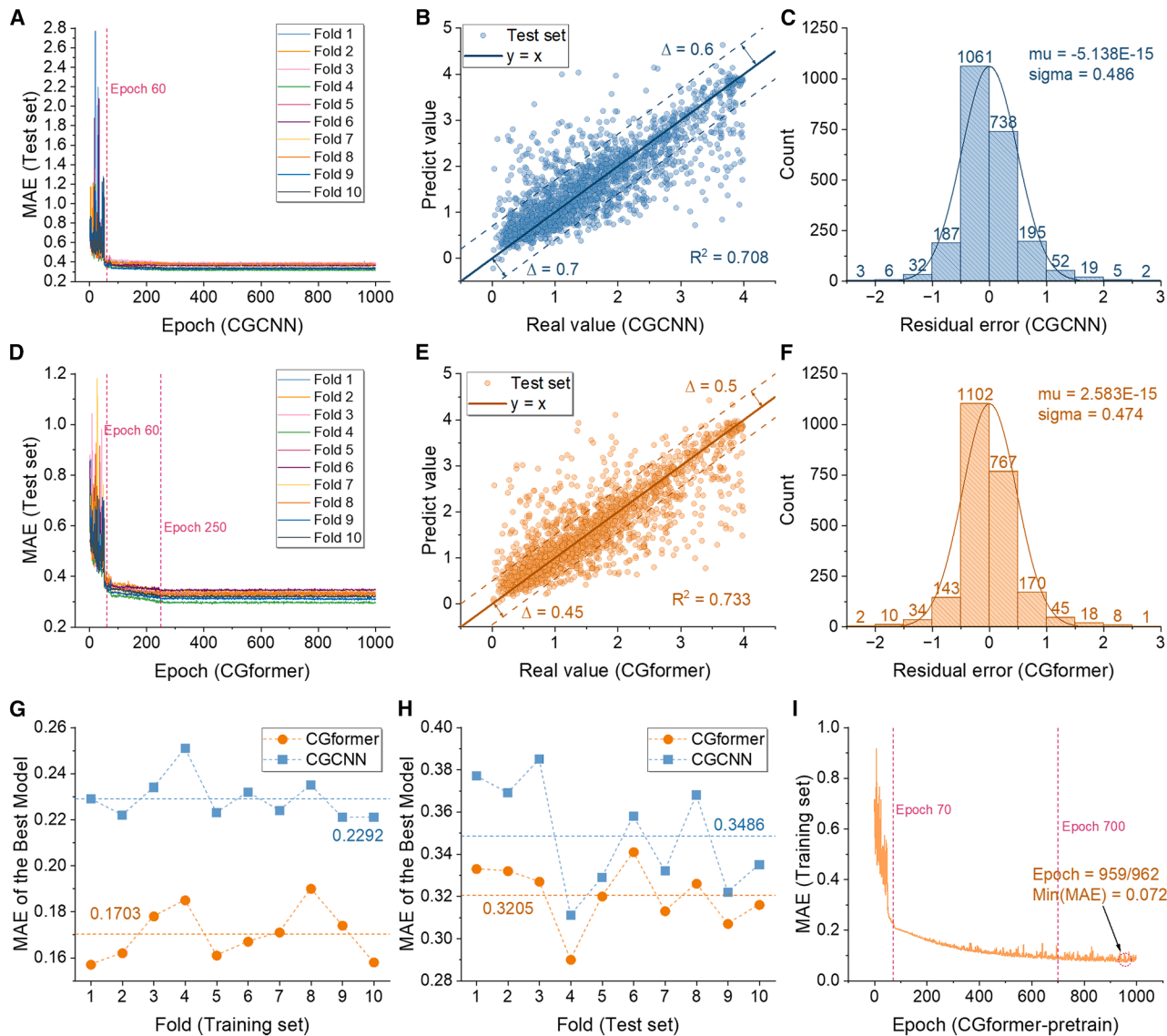
results of unsupervised clustering. To better assess the properties of HE-NSEs within  $G_{13}$ , this study first pre-trains the newly developed CGformer network on an accumulated Na-ion  $E_b$  dataset, enabling the model to effectively learn graph information related to Na-containing structures. Subsequently, the pre-trained model is fine-tuned on the newly calculated HE-NSE dataset of 238 structures, allowing the model to specialize in predicting  $E_b$  for HE-NSEs and aiding in subsequent evaluations. Figures S4 and S5 display the distribution of the training dataset and the calculated  $E_b$  dataset, respectively. It is observed that the calculated  $E_b$  dataset primarily ranges between 0.6 and 1.0 eV and follows a normal distribution, aligning well with the most frequent interval of the pre-trained dataset. The two datasets have a great correlation, and this shows that these structures have great potential as SSEs.

Figure 4 primarily compares the performance of CGformer and the CGCNN on the pre-trained dataset. Figures 4A and 4D show the mean absolute error (MAE) curves for the CGCNN and CGformer after 1,000 training iterations, respectively. Different colored curves represent the results of 10-fold cross-validation (CV), and the red dashed lines indicate significant change points. The high degree of overlap in the CV suggests a reasonable data distribution and strong fitting capabilities of both networks. Notably, CGformer exhibits significantly lower initial errors and

fluctuations compared to the CGCNN, indicating greater stability. Additionally, both networks show a marked decrease in MAE around the 60th epoch, with CGformer continuing to decrease the MAE further at the 250th epoch, resulting in CGformer outperforming the CGCNN in predictive accuracy.

Figures 4B and 4E illustrate the comparison between predicted and actual  $E_b$  values on the test sets during CV for the CGCNN and CGformer, respectively. The solid lines represent the  $y = x$  line, while the dashed lines indicate the degree of prediction deviation. It is apparent that CGformer exhibits significantly smaller prediction deviations than the CGCNN, and CGformer also achieves a higher coefficient of determination ( $R^2$ ) value, demonstrating the superior performance of the newly proposed CGformer architecture. Figures 4C and 4F show the residual plots for the CGCNN and CGformer, respectively, revealing that CGformer's residuals are more tightly clustered around zero. The fitted normal distribution curves indicate that the standard deviation of CGformer's residuals is smaller compared to that of the CGCNN, further validating the enhanced predictive capability of CGformer.

Figures 4G and 4H display the results of the best models from 10-fold CV for CGformer and the CGCNN on the training and test sets, respectively. The dashed lines represent the average MAE from CV. CGformer achieves an average MAE



**Figure 4. Comparison diagram of the effects of CGformer and CGCNN**

(A and D) MAE training curves of CGCNN (A) and CGformer (D) on the test set with 10-fold cross-validation.

(B and E) Plot comparing the predicted and true values of CGCNN (B) and CGformer (E) on the test set with 10-fold cross-validation.

(C and F) Residual plots of CGCNN (C) and CGformer (F).

(G and H) MAE comparison plot of the best models of CGCNN and CGformer on training (G) and test (H) sets with 10-fold cross-validation.

(I) Pre-trained rendering of CGformer on all data.

of only 0.1703 on the training set, improving the CGCNN's performance by 25.7%, and an average MAE of 0.3205 on the test set, which is nearly a 10% improvement over the CGCNN. These results confirm the excellent performance of the CGformer architecture, demonstrating that considering the relationships between nodes in crystal graphs significantly enhances model performance (detailed MAE values for each fold on the training and test sets are provided in Tables S5 and S6). Figure 4I shows the MAE curve for CGformer trained over 1,000 epochs on all data, with noticeable inflection points at the 70th and 700th epochs. The final pre-trained MAE de-

creases to only 0.072. Additional discussions on results at different training epochs are provided in Note S5, with relevant results shown in Figures S6–S8 and Tables S7 and S8, along with justifications for the chosen number of training epochs. In addition, the ALIGNN and SchNet models were also trained separately and compared with CGformer on the dataset. The results further confirmed the excellent properties of CGformer. The analysis of the model and related discussions can be found in Figure S9 and Note S6.

Figure 5 presents the results of fine-tuning CGformer on the calculated  $E_b$  dataset. Building on the robust pre-training

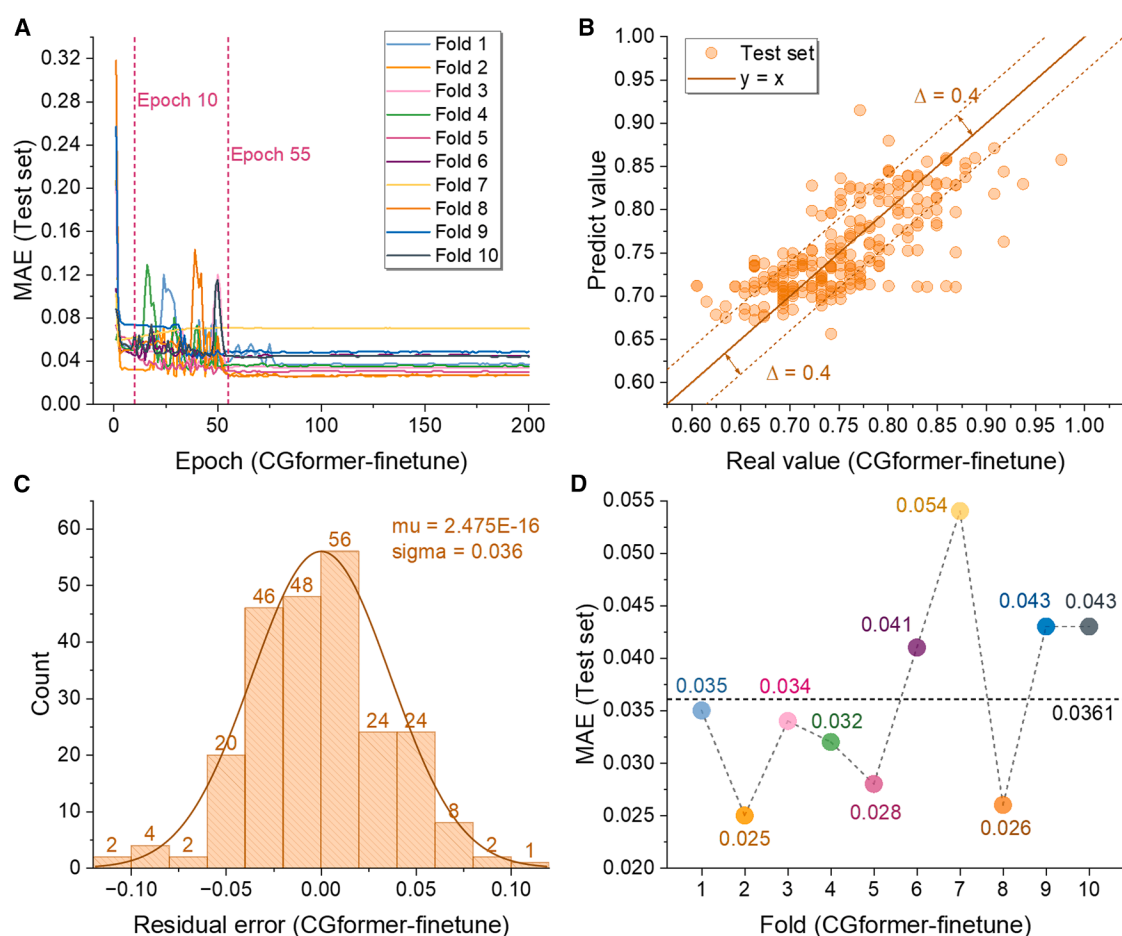


**Figure 5. Diagram of fine-tune results of CGformer on the calculated high-entropy sodium  $E_b$  dataset**

- (A) MAE training curves of CGformer on the test set with 10-fold cross-validation.
- (B) Plot comparing the predicted and true values of CGformer on the test set with 10-fold cross-validation.
- (C) Residual plots of CGformer.
- (D) MAE plot of the best models of CGformer on test sets with 10-fold cross-validation.

foundation, the model is fine-tuned for 200 epochs. As shown in Figure 5A, unlike the pre-training phase, the model exhibited a significant decrease in MAE around the 10th epoch, followed by noticeable perturbations, and another decline around the 55th epoch. This behavior indicates that pre-training is highly beneficial for conserving computational resources. Figures 5B and 5C demonstrate the results after fine-tuning the CGformer model, where the deviations between predicted and actual values are noticeably reduced, and the residuals are mainly confined within the range of  $-0.05$  to  $0.05$ . The high degree of normal distribution aggregation further confirms that CGformer achieved excellent fitting on the calculated  $E_b$  dataset. Figure 5D displays the 10-fold CV results on this dataset, with the black dashed line indicating the average MAE. The CV average MAE is only 0.0361, substantiating the exceptional performance of CGformer. Additionally, Figure S10 supplements these findings by showing the MAE curves during fine-tuning on the computed dataset, where the model achieves good convergence from the 194th epoch.

The application of unsupervised learning combined with the CGformer architecture effectively leverages limited data to achieve high prediction accuracy, thereby enhancing the efficiency and reliability of discovering high-performance superionic conductors in HE-NSEs.

#### Experimental verification

After the CGformer model had been optimized to predict the  $E_b$  with maximum accuracy, a complementary model was developed to evaluate the thermal stability of each candidate. To that end, all Na-containing structures in the Materials Project were mined for their energy above hull ( $E_{\text{hull}}$ ) and compiled into a dedicated training set; the performance of this  $E_{\text{hull}}$  predictor and the associated methodological details are presented in Figure S11 and Note S7.

The trained models were then applied to every HE-NSE in the  $G_{13}$  chemical space, generating ranked lists of predicted  $E_b$  and  $E_{\text{hull}}$  values (complete data are in Table S9). HE-NSEs whose predicted  $E_b$  fell below the median of the original calculated dataset

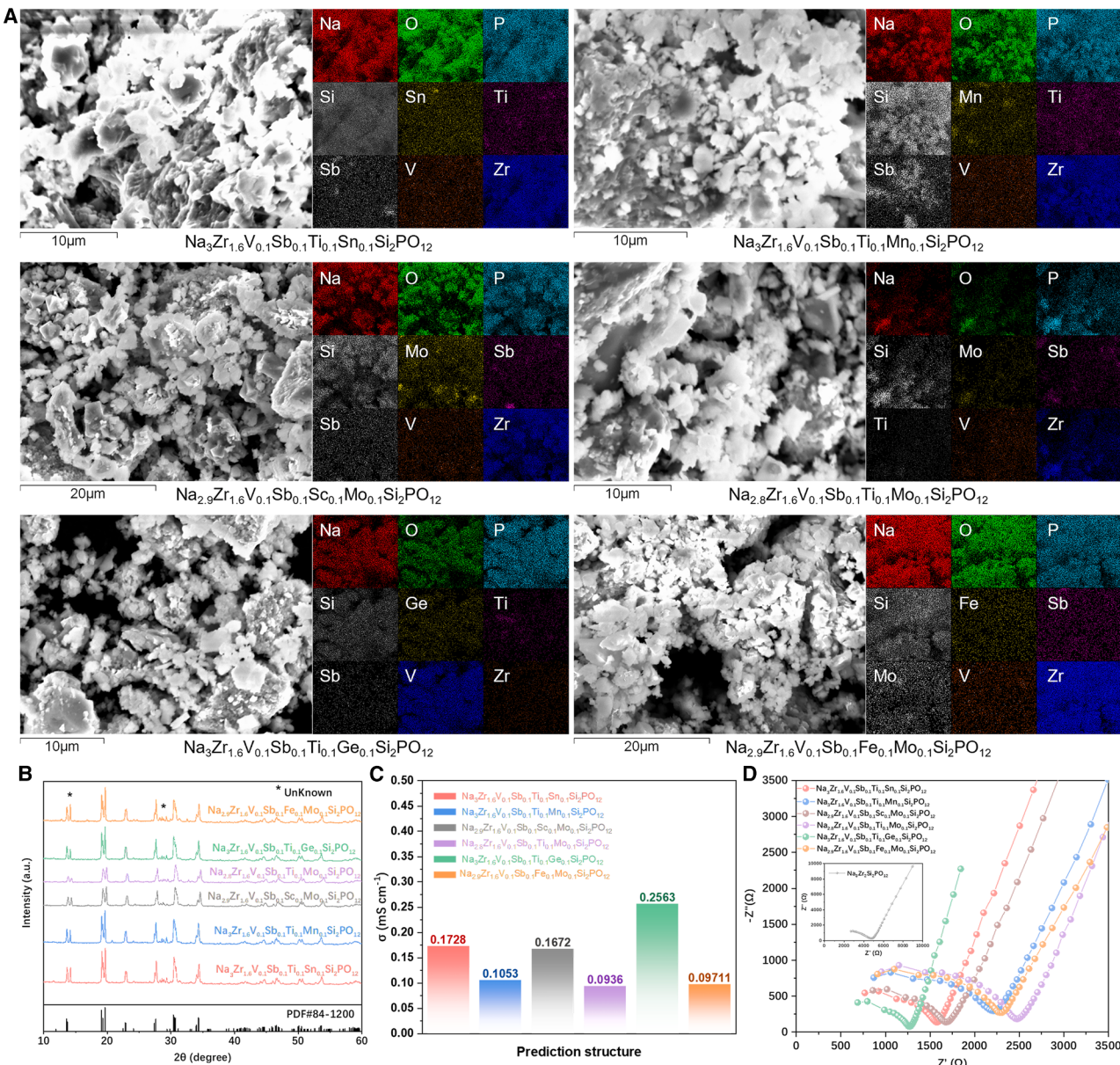


**Figure 6. Experimental validation of the selected HE-NSEs**

(A) SEM images with EDS maps showing uniform distribution of all constituent elements.

(B) Powder X-ray diffraction (XRD) patterns matching the rhombohedral NASICON reference.

(C) Room temperature  $\text{Na}^+$  ionic conductivities, all in the  $10^{-4} \text{ S cm}^{-1}$  range.

(D) Nyquist plots confirming predominantly ionic transport and lower resistance than undoped  $\text{Na}_3\text{Zr}_2\text{Si}_2\text{PO}_{12}$  (inset).

were first retained. From this subset, the ten HE-NSEs with the lowest predicted  $E_{\text{hull}}$ —that is, the highest intrinsic thermodynamic stability—were selected and are summarized in Table S10. Finally, the six structures that combined the lowest  $E_b$  values within that top-ten subset were synthesized by solid-state reaction and electrochemically characterized. Their structural and transport properties are reported in Figure 6.

Figure 6 provides the crucial experimental validation that the six HE-NSEs selected by the combined  $E_b/E_{\text{hull}}$  screening really

form the intended single-phase NASICON lattice and deliver the enhanced transport properties predicted by the CGformer model. The scanning electron microscopy (SEM)/energy dispersive spectroscopy (EDS) mapping panels in secondary-electron micrographs show that all powders consist of angular or plate-like crystallites with typical diameters in the 0.5–3  $\mu\text{m}$  range. Nine-channel EDS mappings collected from exactly the same areas reveal that Na, O, P, Si, Zr, and the co-doping elements (Sn, Mn, Sc, Mo, Ge, or Fe) generate signals that are

spatially co-extensive with the host grains. Within the resolution of the measurement ( $\approx 10 \mu\text{m}$  pixel size), no large segregated regions or element-depleted zones are discernible, indicating that the targeted multi-component chemistry is successfully accommodated throughout the particle ensemble (Figure 6A). This homogeneous distribution is a fingerprint of extensive configurational mixing and proves that the high-entropy design principles assumed by the CGformer input are experimentally realizable.

The powder X-ray diffraction patterns in Figure 6B can all be indexed to the rhombohedral NASICON reference pattern (#84-1200), as evidenced by the coincidence of the experimental reflections with the reference tick marks shown at the bottom of the image. No peak splitting or systematic 20 shift (features that would indicate symmetry reduction or large-scale lattice distortion) is observed.

Bar charts derived from impedance measurements (Figure 6C) place the  $25^\circ\text{C}$  ionic  $\sigma$  between 0.093 and  $0.256 \text{ mS cm}^{-1}$ ; all values lie in the  $10^{-4} \text{ S cm}^{-1}$  range, substantially higher than undoped  $\text{Na}_3\text{Zr}_2\text{Si}_2\text{PO}_{12}$  (see reference trace in the inset of Figure 6D). The Nyquist plots (Figure 6D) feature depressed semicircles followed by nearly vertical low-frequency spikes, the textbook signature of predominantly ionic transport with modest grain-boundary contributions. The overall resistance of each HE-NSE is far lower than that of the NASICON baseline shown in the inset, corroborating the  $\sigma$  ranking extracted from Figure 6C.

In addition, first-principles simulations were carried out for the six HE-NSEs. CI-NEB calculations quantified the  $\text{Na}^+$  migration pathways and activation barriers, whereas AIMD trajectories confirmed their thermal stability at room temperature. The computed diffusion coefficients and structural robustness agree with the experimental observations, thereby providing further support for the effectiveness of the high-entropy materials-design framework proposed in this work. Full computational details are compiled in Figures S12–S15, Table S11, and Notes S8 and S9. Taking these results together, Figure 6 demonstrates two key facts: (1) all six CGformer-predicted HE-NSE formulations are experimentally accessible by conventional solid-state synthesis and (2) every composition exhibits comparatively high room temperature  $\text{Na}^+ \sigma$  accompanied by favorable impedance responses. These observations constitute direct evidence that the computationally selected candidates satisfy both the structural and functional targets set by our modeling strategy.

Furthermore, we performed additional CI-NEB calculations on the poorly predicted structures in  $G_{13}$  and those within other underperforming groups ( $G_1$  and  $G_{17}$ ) for comparative purposes. The results demonstrate that our proposed screening framework for complex crystal structures, combined with the CGformer, can effectively assist researchers in rapidly evaluating structural properties. The relevant supplementary explanations are provided in Figure S16, Tables S12 and S13, and Note S10.

## DISCUSSION

This study addresses the challenge of efficiently identifying HE-NSEs with low  $E_b$  amid limited data and structural complexity. To overcome these issues, an AI-driven prediction workflow has

been developed, integrating unsupervised hierarchical clustering with the novel CGformer model. Specifically, CGformer is pre-trained on a comprehensive Na-ion  $E_b$  dataset and subsequently fine-tuned on a newly calculated dataset of 238 HE-NSEs, enabling precise predictions of  $E_b$  for high-entropy NASICON frameworks. This methodology initially surveys 148,995 potential high-entropy compositions; after removing unsuitable dopants and enforcing ionic-radius/charge-balance constraints, 826 viable structures are retained. Unsupervised clustering categorizes these into 20 groups, from which 238 structures are sampled for  $E_b$  calculations. The  $G_{13}$  cluster emerges as the most promising, containing 18 structures with the highest proportion of low  $E_b$  values. Utilizing the fine-tuned CGformer in conjunction with an  $E_{\text{hull}}$ -based thermodynamic-stability predictor, six top candidates were successfully synthesized and extensively characterized by X-ray diffraction, SEM/EDS mapping, and impedance spectroscopy, which confirmed their single-phase NASICON structure and room temperature conductivities of up to  $0.256 \text{ mS cm}^{-1}$ .

Several key innovations are highlighted in this work: (1) the integration of Graphomer with the CGCNN enables high-accuracy predictions despite limited data, significantly enhancing the model's reliability and generalization capabilities. (2) Additionally, the combination of unsupervised clustering together with an experimental-first validation strategy ensures the selection of structurally robust and high-performance HE-NSEs. (3) Six HE-NSEs predicted by the CGformer model are successfully synthesized and experimentally confirmed to possess high Na-ion  $\sigma$ , a result that validates the predictive power of the model. (4) Moreover, the identification of 18 promising HE-NSEs within the  $G_{13}$  cluster underscores the efficacy of the multi-step screening process in pinpointing viable candidates for SSE applications. (5) Our proposed AI-driven workflow significantly aids in the screening of high-entropy material systems, providing a valuable framework for subsequent research and development in high-entropy materials. CGformer could be further evaluated on additional datasets and augmented with uncertainty-quantification and error-propagation analyses, which would enhance the robustness and broader applicability of its predictions.

In conclusion, CGformer stands at the core of our AI framework, delivering SOTA predictive accuracy that unlocks rapid discovery of high-performance solid electrolytes. By capturing long-range atomic interactions with global attention, CGformer not only pinpoints top-tier  $\text{Na}^+$  conductors now validated in the laboratory but also establishes a versatile platform for accelerated screening of next-generation materials. This capability promises safer, higher-energy solid-state batteries and offers a transferable toolset for breakthroughs across the wider landscape of energy-storage and functional-material research.

## METHODS

### First-principles calculations

DFT calculations are performed using the Vienna Ab initio Simulation Package (VASP).<sup>46</sup> The interactions between ions and electrons are modeled utilizing the projector augmented wave (PAW) method,<sup>47,48</sup> and the Perdew-Burke-Ernzerhof (PBE)

functional within the generalized gradient approximation (GGA)<sup>49</sup> is employed to account for exchange-correlation effects. To accurately capture van der Waals interactions, the DFT-D3 correction method is applied.<sup>50</sup>

A plane-wave basis set with a cutoff energy of 520 eV is used to balance computational efficiency with accuracy. Structural optimizations are carried out until the energy convergence is below  $10^{-5}$  eV and the forces on the atoms are less than 0.01 eV/Å. For the calculation of the  $E_b$  of Na ions in HE-NSEs, the method of CI-NEB is used to find the transition states and determine the final  $E_b$ .

### Unsupervised learning

Unsupervised learning in this study is implemented using a bottom-up hierarchical clustering algorithm (agglomerative hierarchical clustering [AHC]), with the dendrogram generated via the SciPy<sup>51</sup> software package. In AHC, the similarity between samples is quantified using a similarity measure, and pairs of samples are iteratively merged to form new clusters. This process builds a tree-like structure from the bottom up, where each leaf node represents an individual sample and each non-leaf node represents a cluster formed by the similarity of its constituent groups.

For this work, the Euclidean distance is employed as the similarity measure between every two HE-NSEs, and average linkage is used to assess the population differences between clusters. AHC offers the significant advantage of generating the entire clustering hierarchy in a single process. Once the dendrogram is obtained, clustering results can be directly derived based on the tree structure without recalculating the data point assignments for different numbers of clusters. Additionally, AHC facilitates the extraction of multi-level clustering structures with varying granularities by adjusting relevant parameters. In terms of clustering shape, AHC is versatile, accommodating arbitrary cluster shapes and exhibiting insensitivity to the order of input samples.

### Lateral transfer learning

Transfer learning aims to minimize the reliance on large labeled datasets for the target task by sharing knowledge across related domains. Specifically, transfer learning addresses scenarios where the source and target domains share a similar feature space but differ in data distribution. The objective is to utilize existing knowledge—such as models, features, or representations—from the source domain to enhance the learning process in the target domain, thereby improving the performance of the target task. Unlike direct application, the knowledge acquired from the source domain requires adjustment or adaptation to be effective for the target domain.

In this study, transfer learning is employed to address the challenge of limited data in predicting  $E_b$  for HE-NSEs. Specifically, a model trained on a comprehensive dataset of Na-ion  $E_b$  (source task) is adapted for predicting  $E_b$  in HE-NSEs (target task). Given the relatively small size of the HE-NSE  $E_b$  dataset, the model is initially pre-trained on the extensive Na-ion  $E_b$  dataset to effectively learn features associated with Na-containing structures. Subsequently, the pre-trained model undergoes fine-tuning using the limited HE-NSE  $E_b$  data, thereby enhancing its performance in predicting  $E_b$  for HE-NSEs.

### RESOURCE AVAILABILITY

#### Lead contact

Requests for further information and resources should be directed to and will be fulfilled by the lead contact, Jinjin Li ([lijinjin@sjtu.edu.cn](mailto:lijinjin@sjtu.edu.cn)).

#### Materials availability

This study did not generate new unique reagents.

#### Data and code availability

- Na-ion solid electrolyte data reported in this paper will be shared by the lead contact upon request ([http://www.aimslab.cn/#/query\\_na\\_solid\\_electrolyte](http://www.aimslab.cn/#/query_na_solid_electrolyte)).
- All original code has been deposited at GitHub and is publicly available at <https://github.com/taokehao/CGformer> as of the date of publication.
- Any additional information required to reanalyze the data reported in this paper is available from the lead contact upon request.

### ACKNOWLEDGMENTS

The work is supported by the National Key New Materials R&D Program of China (no. 2024ZD0607400), the National Natural Science Foundation of China (no. 32301040), and the Shanghai Science and Technology Project (nos. 24010700100, 21JC1403400, and 23JC1402300).

### AUTHOR CONTRIBUTIONS

Conceptualization, K.T., Jiacong Li, W.H., A.C., Fuqiang Huang, and Jinjin Li; methodology, K.T., Jiacong Li, W.H., A.C., Fuqiang Huang, and Jinjin Li; visualization, K.T., Jiacong Li, and Y.H.; data curation, K.T.; writing – original draft, K.T.; chart illustration, Feiming Huang; resources, Fuqiang Huang and Jinjin Li; supervision, Fuqiang Huang and Jinjin Li; writing – review & editing, Fuqiang Huang and Jinjin Li.

### DECLARATION OF INTERESTS

The authors declare no competing interests.

### SUPPLEMENTAL INFORMATION

Supplemental information can be found online at <https://doi.org/10.1016/j.matt.2025.102380>.

Received: January 23, 2025

Revised: April 17, 2025

Accepted: July 25, 2025

### REFERENCES

1. Mirkhalaf, M., and Rafsanjani, A. (2023). Harnessing machine mechanisms to continuously reprogram metamaterials. *Matter* 6, 3719–3731. <https://doi.org/10.1016/j.matt.2023.08.020>.
2. Darvish, K., Skreta, M., Zhao, Y., Yoshikawa, N., Som, S., Bogdanovic, M., Cao, Y., Hao, H., Xu, H., Aspuru-Guzik, A., et al. (2025). ORGAN: A robotic assistant for automated chemistry experimentation and characterization. *Matter* 8, 101897. <https://doi.org/10.1016/j.matt.2024.10.015>.
3. Park, D., Chung, W., Min, B.K., Lee, U., Yu, S., and Kim, K. (2024). Computational screening of sodium solid electrolytes through unsupervised learning. *npj Comput. Mater.* 10, 226. <https://doi.org/10.1038/s41524-024-01392-6>.
4. Tang, Y., Zhang, Q., Zuo, W., Zhou, S., Zeng, G., Zhang, B., Zhang, H., Huang, Z., Zheng, L., Xu, J., et al. (2024). Sustainable layered cathode with suppressed phase transition for long-life sodium-ion batteries. *Nat. Sustain.* 7, 348–359. <https://doi.org/10.1038/s41893-024-01288-9>.

5. Chang, Y., Benlolo, I., Bai, Y., Reimer, C., Zhou, D., Zhang, H., Matsumura, H., Choubisa, H., Li, X.-Y., Chen, W., et al. (2024). High-entropy alloy electrocatalysts screened using machine learning informed by quantum-inspired similarity analysis. *Matter* 7, 4099–4113. <https://doi.org/10.1016/j.matt.2024.10.001>.
6. Zeng, Y., Ouyang, B., Liu, J., Byeon, Y.-W., Cai, Z., Miara, L.J., Wang, Y., and Ceder, G. (2022). High-entropy mechanism to boost ionic conductivity. *Science* 378, 1320–1324. <https://doi.org/10.1126/science.abq1346>.
7. Ma, B., Zhang, L., Wang, W., Yu, H., Yang, X., Chen, S., Wang, H., and Liu, X. (2024). Application of deep learning for informatics aided design of electrode materials in metal-ion batteries. *Green Energy Environ.* 9, 877–889. <https://doi.org/10.1016/j.gee.2022.10.002>.
8. Chen, A., Wang, Z., Vidaurre, K.L.L., Han, Y., Ye, S., Tao, K., Wang, S., Gao, J., and Li, J. (2024). Knowledge-reused transfer learning for molecular and materials science. *J. Energy Chem.* 98, 149–168. <https://doi.org/10.1016/j.jecm.2024.06.013>.
9. Wang, Z., Zhang, H., Ren, J., Lin, X., Han, T., Liu, J., and Li, J. (2021). Predicting adsorption ability of adsorbents at arbitrary sites for pollutants using deep transfer learning. *npj Comput. Mater.* 7, 19. <https://doi.org/10.1038/s41524-021-00494-9>.
10. Xie, T., and Grossman, J.C. (2018). Crystal Graph Convolutional Neural Networks for an Accurate and Interpretable Prediction of Material Properties. *Phys. Rev. Lett.* 120, 145301. <https://doi.org/10.1103/PhysRevLett.120.145301>.
11. Choudhary, K., and DeCost, B. (2021). Atomistic Line Graph Neural Network for improved materials property predictions. *npj Comput. Mater.* 7, 185. <https://doi.org/10.1038/s41524-021-00650-1>.
12. Schütt, K.T., Sauceda, H.E., Kindermans, P.-J., Tkatchenko, A., and Müller, K.-R. (2018). SchNet – A deep learning architecture for molecules and materials. *J. Chem. Phys.* 148, 241722. <https://doi.org/10.1063/1.5019779>.
13. Zhao, C., Liu, L., Qi, X., Lu, Y., Wu, F., Zhao, J., Yu, Y., Hu, Y.-S., and Chen, L. (2018). Solid-State Sodium Batteries. *Adv. Energy Mater.* 8, 1703012. <https://doi.org/10.1002/aenm.201703012>.
14. Bai, Z., Yao, Q., Wang, M., Meng, W., Dou, S., Liu, H.k., and Wang, N. (2024). Low-Temperature Sodium-Ion Batteries: Challenges and Progress. *Adv. Energy Mater.* 14, 2303788. <https://doi.org/10.1002/aenm.202303788>.
15. Huang, J., Wu, K., Xu, G., Wu, M., Dou, S., and Wu, C. (2023). Recent progress and strategic perspectives of inorganic solid electrolytes: fundamentals, modifications, and applications in sodium metal batteries. *Chem. Soc. Rev.* 52, 4933–4995. <https://doi.org/10.1039/D2CS01029A>.
16. Li, J., Zhou, M., Wu, H.-H., Wang, L., Zhang, J., Wu, N., Pan, K., Liu, G., Zhang, Y., Han, J., et al. (2024). Machine Learning-Assisted Property Prediction of Solid-State Electrolyte. *Adv. Energy Mater.* 14, 2304480. <https://doi.org/10.1002/aenm.202304480>.
17. Wang, C., Kim, J.T., Wang, C., and Sun, X. (2023). Progress and Prospects of Inorganic Solid-State Electrolyte-Based All-Solid-State Pouch Cells. *Adv. Mater.* 35, 2209074. <https://doi.org/10.1002/adma.202209074>.
18. Fan, P., Liu, H., Marosz, V., Samuels, N.T., Suib, S.L., Sun, L., and Liao, L. (2021). High Performance Composite Polymer Electrolytes for Lithium-Ion Batteries. *Adv. Funct. Mater.* 31, 2101380. <https://doi.org/10.1002/adfm.202101380>.
19. Zhou, X., Wang, Y., Gu, Y., Su, J., Liu, Y., Yin, Y., Yuan, S., Ma, J., Jin, Z., and Zuo, J.-L. (2024). All-purpose redox-active metal-organic frameworks as both cathodic and anodic host materials for advanced lithium-sulfur batteries. *Matter* 7, 3069–3082. <https://doi.org/10.1016/j.matt.2024.04.039>.
20. Schwietert, T.K., Arszelewski, V.A., Wang, C., Yu, C., Vasileiadis, A., de Klerk, N.J.J., Hageman, J., Hupfer, T., Kerkamm, I., Xu, Y., et al. (2020). Clarifying the relationship between redox activity and electrochemical stability in solid electrolytes. *Nat. Mater.* 19, 428–435. <https://doi.org/10.1038/s41563-019-0576-0>.
21. Park, H., Kang, M., Lee, D., Park, J., Kang, S.J., and Kang, B. (2024). Activating reversible carbonate reactions in Nasicon solid electrolyte-based Na-air battery via in-situ formed catholyte. *Nat. Commun.* 15, 2952. <https://doi.org/10.1038/s41467-024-47415-0>.
22. Wang, J., He, T., Yang, X., Cai, Z., Wang, Y., Lacivita, V., Kim, H., Ouyang, B., and Ceder, G. (2023). Design principles for NASICON super-ionic conductors. *Nat. Commun.* 14, 5210. <https://doi.org/10.1038/s41467-023-40669-0>.
23. Liu, Y., Rong, X., Bai, R., Xiao, R., Xu, C., Zhang, C., Xu, J., Yin, W., Zhang, Q., Liang, X., et al. (2023). Identifying the intrinsic anti-site defect in manganese-rich NASICON-type cathodes. *Nat. Energy* 8, 1088–1096. <https://doi.org/10.1038/s41560-023-01301-z>.
24. Chen, M., Hua, W., Xiao, J., Cortie, D., Chen, W., Wang, E., Hu, Z., Gu, Q., Wang, X., Indris, S., et al. (2019). NASICON-type air-stable and all-climate cathode for sodium-ion batteries with low cost and high-power density. *Nat. Commun.* 10, 1480. <https://doi.org/10.1038/s41467-019-09170-5>.
25. Jian, Z., Hu, Y.-S., Ji, X., and Chen, W. (2017). NASICON-Structured Materials for Energy Storage. *Adv. Mater.* 29, 1601925. <https://doi.org/10.1002/adma.201601925>.
26. Zheng, F., Kotobuki, M., Song, S., Lai, M.O., and Lu, L. (2018). Review on solid electrolytes for all-solid-state lithium-ion batteries. *J. Power Sources* 389, 198–213. <https://doi.org/10.1016/j.jpowsour.2018.04.022>.
27. Lu, Y., Li, L., Zhang, Q., Niu, Z., and Chen, J. (2018). Electrolyte and Interface Engineering for Solid-State Sodium Batteries. *Joule* 2, 1747–1770. <https://doi.org/10.1016/j.joule.2018.07.028>.
28. Sun, Y., Gao, X., Ma, T., and Zhang, J. (2024). High-performance Na-S batteries enabled by a chemical and spatial dual-confinement strategy. *Matter* 7, 1920–1922. <https://doi.org/10.1016/j.matt.2024.04.012>.
29. Zhang, R., Wang, C., Zou, P., Lin, R., Ma, L., Yin, L., Li, T., Xu, W., Jia, H., Li, Q., et al. (2022). Compositionally complex doping for zero-strain zero-cobalt layered cathodes. *Nature* 610, 67–73. <https://doi.org/10.1038/s41586-022-05115-z>.
30. Wang, J., Dreyer, S.L., Wang, K., Ding, Z., Diemant, T., Karkera, G., Ma, Y., Sarkar, A., Zhou, B., Gorbunov, M.V., et al. (2022). P2-type layered high-entropy oxides as sodium-ion cathode materials. *Mater. Futur.* 1, 035104. <https://doi.org/10.1088/2752-5724/ac8ab9>.
31. Qi, H., Chen, L., Deng, S., and Chen, J. (2023). High-entropy ferroelectric materials. *Nat. Rev. Mater.* 8, 355–356. <https://doi.org/10.1038/s41578-023-00544-2>.
32. Schweidler, S., Botros, M., Strauss, F., Wang, Q., Ma, Y., Velasco, L., Cadilha Marques, G., Sarkar, A., Kübel, C., Hahn, H., et al. (2024). High-entropy materials for energy and electronic applications. *Nat. Rev. Mater.* 9, 266–281. <https://doi.org/10.1038/s41578-024-00654-5>.
33. Ding, F., Zhao, C., Xiao, D., Rong, X., Wang, H., Li, Y., Yang, Y., Lu, Y., and Hu, Y.-S. (2022). Using High-Entropy Configuration Strategy to Design Na-Ion Layered Oxide Cathodes with Superior Electrochemical Performance and Thermal Stability. *J. Am. Chem. Soc.* 144, 8286–8295. <https://doi.org/10.1021/jacs.2c02353>.
34. Fu, F., Liu, X., Fu, X., Chen, H., Huang, L., Fan, J., Le, J., Wang, Q., Yang, W., Ren, Y., et al. (2022). Entropy and crystal-facet modulation of P2-type layered cathodes for long-lasting sodium-based batteries. *Nat. Commun.* 13, 2826. <https://doi.org/10.1038/s41467-022-30113-0>.
35. Zhao, C., Ding, F., Lu, Y., Chen, L., and Hu, Y.-S. (2020). High-Entropy Layered Oxide Cathodes for Sodium-Ion Batteries. *Angew. Chem. Int. Ed. Engl.* 59, 264–269. <https://doi.org/10.1002/anie.201912171>.
36. He, B., Ye, A., Chi, S., Mi, P., Ran, Y., Zhang, L., Zou, X., Pu, B., Zhao, Q., Zou, Z., et al. (2020). CAVD, towards better characterization of void space for ionic transport analysis. *Sci. Data* 7, 153. <https://doi.org/10.1038/s41597-020-0491-x>.
37. Adams, S., and Rao, R.P. (2011). High power lithium ion battery materials by computational design. *physica status solidi (a)* 208, 1746–1753. <https://doi.org/10.1002/pssa.201001116>.

38. Park, K.-H., Kaup, K., Assoud, A., Zhang, Q., Wu, X., and Nazar, L.F. (2020). High-Voltage Superionic Halide Solid Electrolytes for All-Solid-State Li-Ion Batteries. *ACS Energy Lett.* 5, 533–539. <https://doi.org/10.1021/acsenergylett.9b02599>.
39. Li, X., Xu, J., Li, H., Zhu, H., Guo, S., and Zhou, H. (2022). Synergetic Anion–Cation Redox Ensures a Highly Stable Layered Cathode for Sodium-Ion Batteries. *Adv. Sci.* 9, 2105280. <https://doi.org/10.1002/advs.202105280>.
40. Dalla-Torre, H., Gonzalez, L., Mendoza-Revilla, J., Lopez Carranza, N., Grzywaczewski, A.H., Oteri, F., Dallago, C., Trop, E., de Almeida, B.P., Sir-elkhaim, H., et al. (2025). Nucleotide Transformer: building and evaluating robust foundation models for human genomics. *Nat. Methods* 22, 287–297. <https://doi.org/10.1038/s41592-024-02523-z>.
41. Tibo, A., He, J., Janet, J.P., Nittinger, E., and Engkvist, O. (2024). Exhaustive local chemical space exploration using a transformer model. *Nat. Commun.* 15, 7315. <https://doi.org/10.1038/s41467-024-51672-4>.
42. Diaz, D.J., Gong, C., Ouyang-Zhang, J., Loy, J.M., Wells, J., Yang, D., Ellington, A.D., Dimakis, A.G., and Klivans, A.R. (2024). Stability Oracle: a structure-based graph-transformer framework for identifying stabilizing mutations. *Nat. Commun.* 15, 6170. <https://doi.org/10.1038/s41467-024-49780-2>.
43. Zheng, S., He, J., Liu, C., Shi, Y., Lu, Z., Feng, W., Ju, F., Wang, J., Zhu, J., Min, Y., et al. (2024). Predicting equilibrium distributions for molecular systems with deep learning. *Nat. Mach. Intell.* 6, 558–567. <https://doi.org/10.1038/s42256-024-00837-3>.
44. Lu, S., Gao, Z., He, D., Zhang, L., and Ke, G. (2024). Data-driven quantum chemical property prediction leveraging 3D conformations with Uni-Mol+. *Nat. Commun.* 15, 7104. <https://doi.org/10.1038/s41467-024-51321-w>.
45. Young, A., Röst, H., and Wang, B. (2024). Tandem mass spectrum prediction for small molecules using graph transformers. *Nat. Mach. Intell.* 6, 404–416. <https://doi.org/10.1038/s42256-024-00816-8>.
46. Kresse, G., and Furthmüller, J. (1996). Efficient iterative schemes for ab initio total-energy calculations using a plane-wave basis set. *Phys. Rev. B* 54, 11169–11186. <https://doi.org/10.1103/PhysRevB.54.11169>.
47. Blöchl, P.E. (1994). Projector augmented-wave method. *Phys. Rev. B* 50, 17953–17979. <https://doi.org/10.1103/PhysRevB.50.17953>.
48. Kresse, G., and Joubert, D. (1999). From ultrasoft pseudopotentials to the projector augmented-wave method. *Phys. Rev. B* 59, 1758–1775. <https://doi.org/10.1103/PhysRevB.59.1758>.
49. Perdew, J.P., Burke, K., and Ernzerhof, M. (1996). Generalized Gradient Approximation Made Simple. *Phys. Rev. Lett.* 77, 3865–3868. <https://doi.org/10.1103/PhysRevLett.77.3865>.
50. Lee, K., Murray, É.D., Kong, L., Lundqvist, B.I., and Langreth, D.C. (2010). Higher-accuracy van der Waals density functional. *Phys. Rev. B* 82, 081101. <https://doi.org/10.1103/PhysRevB.82.081101>.
51. Virtanen, P., Gommers, R., Oliphant, T.E., Haberland, M., Reddy, T., Cournapeau, D., Burovski, E., Peterson, P., Weckesser, W., Bright, J., et al. (2020). SciPy 1.0: fundamental algorithms for scientific computing in Python. *Nat. Methods* 17, 261–272. <https://doi.org/10.1038/s41592-019-0686-2>.